


Tunable thermoresponsive $\text{TiO}_2/\text{SiO}_2$ Bragg stacks based on sol–gel fabrication methods

Journal of Intelligent Material Systems and Structures
24(18) 2204–2214
© The Author(s) 2012
Reprints and permissions:
sagepub.co.uk/journalsPermissions.nav
DOI: 10.1177/1045389X12453970
jim.sagepub.com


Ida Pavlichenko^{1,2,*}, Armin T Exner^{3,*}, Paolo Lugli³,
Giuseppe Scarpa³ and Bettina V Lotsch^{1,2}

Abstract

Thermoresponsive $\text{TiO}_2/\text{SiO}_2$ one-dimensional photonic crystals (Bragg stacks) fabricated via sol–gel processing methods represent a promising class of environmentally responsive nanostructures featuring optically encoded temperature and humidity detection. The thermo-optic response of the layer materials is amplified by their inherent porosity owing to adsorption/desorption of ambient humidity into the mesoporous multilayer structure. Based on a comprehensive analysis of the impact of layer thickness, refractive index and thermo-optic coefficient on the stop band position, and width of various Bragg stack architectures, design criteria for thermoresponsive Bragg stacks operating in the visible range of the optical spectrum are put forward. A large and well-defined thermo-optic signature is expected for material combinations featuring individually high thermo-optic coefficients with the same sign or allowing for large changes in the effective refractive indices due to water adsorption in the porous layers reinforcing the thermo-optic response, as observed in the $\text{TiO}_2/\text{SiO}_2$ couple. Important practical aspects of the performance of thermoresponsive Bragg stacks are addressed, including the hysteresis properties of $\text{TiO}_2/\text{SiO}_2$ Bragg stacks during multiple heating/cooling cycles, as well as response and recovery times ($\sim 2\text{--}4$ s) of the multilayer system during external changes in ambient humidity.

Keywords

Photonic crystal, thermo-optic coefficient, Bragg stack, silicon dioxide, titanium dioxide

Introduction

One-dimensional photonic crystals (1D PCs), also known as Bragg stacks (BSs), have recently demonstrated potential for various technological applications such as chemical, physical, and biological sensing, photovoltaics, distributed feedback lasers, radiation shielding, and many others (Calvo et al., 2011, Ge and Yin, 2011, Lotsch et al., 2009, Puzzo et al., 2011, Scotognella et al., 2009). 1D PCs represent a class of multilayer structures possessing a periodic modulation of the refractive index (RI) in one dimension, giving rise to a photonic band gap (stop band) and hence structural color (Joannopoulos et al., 2008). The position and width of the stop band are determined by the periodic dielectric structure and can be tuned by external stimuli inducing changes in the optical thickness of the layers, that is, RI or physical thickness (Bonifacio et al., 2009). A wide arsenal of fabrication methods and numerous combinations of organic and inorganic materials together with surface functionalization and morphology tuning opens up new avenues to the design of simple, yet versatile sensing devices (Patzke et al., 2011;

Redel et al., 2011). For the fabrication of 1D PCs, the sol–gel process has proven a valuable strategy as it enables a relatively simple, fast, and low-cost synthetic pathway to produce dense, nanoparticle (NP)-based or ordered mesoporous thin films with excellent compositional control and homogeneity facilitating the fabrication of uniform crystalline layers. Properties such as thickness, pore size, and surface area of the film can be tailored by the control of sol–gel processing and deposition parameters (Hench and West, 1990;

¹Max Planck Institute for Solid State Research, Stuttgart, Germany

²Chemistry Department and Center for Nanoscience (CeNS), University of Munich (LMU), Munich, Germany

³Institute for Nanoelectronics, Technische Universität München, Munich, Germany

*These two authors made an equal contribution

Corresponding author:

Bettina V Lotsch, Max Planck Institute for Solid State Research, Heisenbergstrasse 1, 70569 Stuttgart, Germany, and Chemistry Department and Center for Nanoscience, University of Munich (LMU), Munich, Germany.
Email: b.lotsch@fkf.mpg.de

Tsuchiya et al., 1994). Along these lines, several deposition methods for the assembly of 1D PCs with high optical and structural quality have been reported, namely, dip-, spin-, and spray-coating methods, as well as layer-by-layer (LbL) assembly protocols that allow for the deposition of multilayer thin films on various substrates in a more facile and cost-efficient manner as compared to physical deposition techniques such as electron beam evaporation or sputter deposition (Inui et al., 2008; Kobler et al., 2009; Nogueira et al., 2011).

BSs composed of $\text{TiO}_2/\text{SiO}_2$ multilayers were studied most extensively during the past years due to the variety of intriguing properties such systems offer. Titanium dioxide is an excellent optical material with high RI (= 1.9–2.5), possessing a high chemical stability and low toxicity (Macwan et al., 2011). Owing to its ultraviolet-induced photocatalytic properties, TiO_2 is used for the degradation of organic pollutants and exhibits fairly good antibacterial activity (Park and Kim, 2002). Thin-film BSs exhibiting structural color have, for instance, been fabricated by means of a LbL deposition process (Lee et al., 2006; Wu et al., 2007) or by spin-coating from NP dispersions (Calvo et al., 2008; Colodrero et al., 2008a). Colodrero et al. (2008b) carried out a comprehensive study on the optical properties of various NP-based 1D PCs versus changes in the ambient vapor pressure and discussed the sorption properties of the constituent layers. Further captivating possibilities, including the fabrication of flexible NP-based Bragg mirrors, embedding of gold NPs into the BS for plasmonic applications and many others were demonstrated recently (Sánchez-Sobrado et al., 2010, 2011). Owing to the intrinsic porosity of sol-gel-processed NP-based multilayers, they are more sensitive toward various analytes and hence possess excellent morphologies for sensing applications.

Apart from various analyte sensing schemes realized with NP-based $\text{TiO}_2/\text{SiO}_2$ BSs owing to their inherent porosity, the thermo-optic properties of TiO_2 render multilayer systems involving TiO_2 layers interesting candidates for temperature sensing applications. A comprehensive description of the most common technologies and a review of materials frequently used for the fabrication of thermo-optic switches have been provided by Coppola et al. (2011). However, the authors do not consider the utilization of 1D porous PCs consisting of materials with a high thermo-optic coefficient (TOC) (e.g. TiO_2) as potential systems for thermo-optic tuning. The TOC of titanium dioxide measured for coatings deposited by electron beam deposition is negative and equal to $-1.77 \times 10^{-4} \text{ K}^{-1}$ between 18°C and 120°C and corresponds to $-3.04 \times 10^{-4} \text{ K}^{-1}$ between 220°C and 325°C at 800 nm (Gülşen and Inci, 2002). The TOC of silicon dioxide is positive with a value around $1 \times 10^{-5} \text{ K}^{-1}$ (Ghosh, 1995). The thermo-optic response of $\text{TiO}_2/\text{SiO}_2$ BSs was recently studied by Pavlichenko et al. (2012). The authors observed

enhancement of the thermal shift induced by ambient humidity, which is adsorbed into the porous layer architecture due to capillary condensation. Nanostructured TiO_2 films lend themselves particularly well for humidity-enhanced temperature tuning due to the high exposed surface area and facilitated water adsorption into the pore system owing to the photo-activated self-cleaning properties of TiO_2 surfaces (Yadav et al., 2007; Tai et al., 2003; Yu et al., 2001). While the stability, and hence performance, of optical filters is reduced by the influence of ambient humidity (Zverev et al., 1981), the thermo-optic response can be greatly enhanced by the presence of humidity. Therefore, NP-based BSs represent a versatile detection platform featuring a convenient and compact optical readout system.

In this article, we elaborate on different aspects pertaining to the temperature and humidity responses of BSs based on a label-free optical readout. The design of periodic multilayer architectures by both experiment and simulations will be outlined based on various design criteria, such as sensitivity and response kinetics. We also discuss important practical aspects of the performance of thermoresponsive BSs including the hysteresis properties of the multilayer system during multiple heating/cooling cycles and the response and recovery times during external changes in ambient humidity.

Methods

Preparation of TiO_2 and SiO_2 suspensions

The suspension of TiO_2 NPs was synthesized as in Lotsch and Ozin (2008). Sonication (37 kHz, S100H; Elmasonic) of the suspension allows obtaining NPs with a hydrodynamic diameter in the range between 7 and 15 nm. SiO_2 colloids were purchased from Sigma-Aldrich (LUDOX SM-30 (size of 7–10 nm), 30 wt% in H_2O and (LUDOX TMA (size of 15–30 nm), 34 wt% in H_2O). Particle size distribution of the precursor TiO_2 and SiO_2 suspensions was analyzed using dynamic light-scattering photocorrelation spectroscopy (Zetasizer Nano ZS; Malvern) at 20°C. The anatase modification of the TiO_2 powder calcined at 350°C for 1 h was confirmed by X-ray diffraction (D8 DISCOVER; Bruker).

Bragg stack assembly

Thermoresponsive PCs were assembled by sequential deposition of TiO_2 and SiO_2 suspensions on a clean ISO 8037/1 glass slide ($2.5 \times 2.5 \text{ cm}^2$) (Pavlichenko et al., 2012). Thin layers of TiO_2 and SiO_2 were produced using the spin-coating technique (WS-650SZ6NPP/LITE; Laurell). The single thin film thickness and porosity were characterized by spectroscopic ellipsometry (performed on a Woollam M200D variable angle ellipsometer in the entire spectral range of 190–1000 nm at

angles of incidence of 65°, 70°, and 75°). Scanning electron microscopy (JSM-6500F, JEOL, operating at an accelerating voltage of 2–5 kV) was used to examine the morphology of the BS cross section and flat surfaces.

Simulations

We carried out the simulations of the transmission spectra with the program COMSOL Multiphysics 3.3, radio frequency (RF) module in a two-dimensional (2D) in-plane transverse electric (TE) waves application mode. In the absence of external currents and sources, Maxwell's equations are represented in the following form (equation (1))

$$\nabla \times (\nabla \times \mathbf{E}(\mathbf{r})) - n^2 k^2 \mathbf{E}(\mathbf{r}) = 0 \quad (1)$$

where \mathbf{E} is the electric field, n is the RI, and k is the free-space wave number. To model the TE waves propagating through the simulated 1D PC, drawn in a 2D geometry as a stack of rectangles with user-defined thicknesses, we switch to a scalar equation (2) for the TE field component E_z

$$-\nabla \cdot \nabla \cdot E_z - n^2 k^2 E_z = 0 \quad (2)$$

To avoid reflection at outer boundaries of the PC geometry, we selected the “matched boundary” conditions, and inside the geometry, we applied the “continuity” boundary condition to each boundary except for the one where the wave is entering the structure. To characterize the transmission coefficient, we calculated the S_{21} scattering parameter (for more details, see COMSOL Multiphysics, 2008).

Optical response and hysteresis analysis

To obtain transmission spectra of the BS in the range of 400–800 nm, we used a monochromator (Cornerstone260 1/4 m; Newport) with a high pressure arc lamp as a light source and a 10×10 -mm calibrated silicon detector connected to a digital lock-in amplifier (Merlin) (Pavlichenko et al., 2012). The temperature of the BS was varied by two Peltier elements, and the PT100 temperature sensor was attached to the other side of the BS above the optical axis. Peltier elements and the temperature sensor were connected to a remote-controlled source meter. A software proportional integral controller regulated the heating and cooling of the Peltier elements. The measured deviation of the temperature during the measurement was less than 0.1°C. For each temperature, the sample was equilibrated for 60 s.

For the hysteresis measurement, the sample was mounted on two Peltier elements as described for the spectral transmission measurements. A standard orange light-emitting diode (LED) (peak wavelength of 604 nm with angular divergence of the light beam

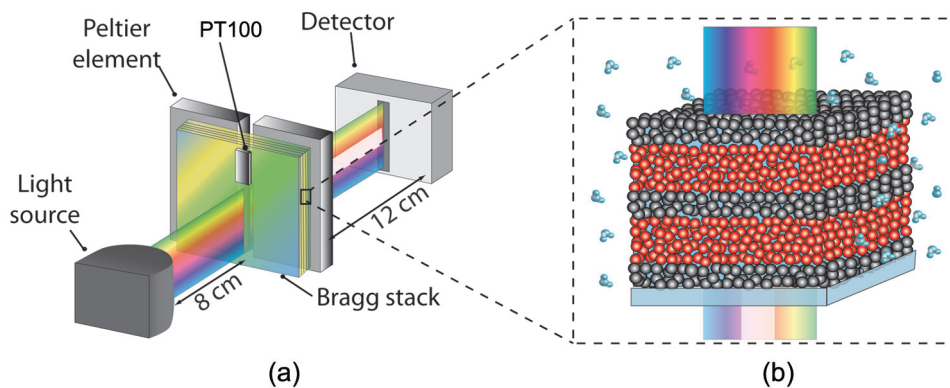
of $\sim 20^\circ$), sourced by a current of 5 mA, was chosen as a light source. The LED was equilibrated before the experiment for 30 min. The LED light beam passed through a monochromator set to the wavelength of 610 nm, to gain a narrower spectrum. For the temperature control, extra care has been taken such that the temperature was neither oscillating nor overshooting the set-point temperature. After the set-point temperature was reached, the sample was equilibrated for another 60 s before the measurement was taken.

For the characterization of response time, we changed the RH of the environment (20%) by introducing water vapor onto the sample surface. The tubing with the nitrogen stream carrying the water vapor was mounted above the surface of the BS. The measured RH of the vapor was 70%; additionally, the valve located on the tubing allowed the instant turning off of the vapor stream. Time-dependent spectroscopy was performed by fiber optic spectrometer (USB2000+; Ocean Optics) integrated with an optical light microscope (DM2500 M; Leica).

Results and discussion

The experimental setup for the characterization of the thermo-optic behavior of NP-based porous BSs under environmental conditions is illustrated in Scheme 1. Temperature tuning of the BS, deposited on a transparent glass substrate, is realized through controlled heating/cooling by means of thermoelectric elements as demonstrated in Scheme 1(a). The BS, acting as a thermoresponsive optical filter, modifies the spectrum of the incident light as a function of temperature (Domash et al., 2003; Hohlfeld and Zappe, 2004). The porous nature of the NP-based multilayers facilitates condensation of ambient humidity in the vicinity of the BS into the pores, thus changing the effective RI of the system (Pavlichenko et al., 2012).

This principle is demonstrated by monitoring the shift of the stop band of a 8.5-bilayer TiO_2 (50 nm)/ SiO_2 (90 nm) BS upon heating under ambient conditions. Since in the previous studies (Pavlichenko et al., 2012), we observed that the largest thermal shift enhancement occurs in the temperature region below 30°C, transmission spectra were measured in the temperature range between 15°C and 25°C with steps of 2°C. The BS was thermally equilibrated for 1 min before taking the measurement. We observed an enhanced blue shift of the transmission spectra during heating due to the combined effects of the thermo-optic RI change and water desorption from the pores of the BS. However, evidently, the temperature-induced shift of the “red” edge of the stop band is significantly larger (20 nm) than that of the “blue” edge (5 nm). Such asymmetric behavior will be rationalized by means of



Scheme 1. (a) Schematic drawing of the experimental setup for humidity-enhanced temperature detection using a 1D PC. The Bragg stack acts as a tunable optical filter for the incident beam, resulting in the observation of the photonic stop band. (b) Enlarged schematic illustration of the Bragg stack in ambient conditions, showing the adsorption/desorption of the water vapor surrounding the BS into the textural pores of the network.

simulation of the stop band position and width upon changing various geometric BS parameters (thickness of the layers) and material properties (RI) as discussed in the following (Figure 2).

In order to design BSs with suitable optical characteristics as well as sensitivity to ambient conditions, we demonstrate how thickness changes and independently RI changes of the low-RI and high-RI materials affect the position and width of the photonic stop band, based on well-established PC concepts (Joannopoulos et al., 2008). Figure 2(a) and (b) shows the influence of the increase in layer thickness from 100 to 140 nm of the low-RI material SiO₂ (RI \approx 1.3) and from 70 to 110 nm of the high-RI material TiO₂ (RI \approx 1.9), respectively, for a 9-bilayer BS TiO₂/SiO₂ in increments of 2 nm. It can be seen that the change in layer thickness of one of the materials results in a shift of the stop band to longer wavelengths, consistent with an increase in optical thickness of a bilayer with increasing physical thickness, while the width of the stop band remains approximately constant. A different behavior is seen in Figure 2(c) and (d), which shows the influence of an increase in RI from 1.1 to 1.5 for SiO₂ and from 1.7 to 2.1 for TiO₂, respectively, while keeping the layer thicknesses constant: 90 nm for TiO₂ and 120 nm for SiO₂. Although only the RI of one material at a time is changed for clarity, the simulations show a substantial effect of changes in the RI on the position and width of the stop band. In general, a larger RI contrast between the two layer materials translates into a larger stop band width and vice versa. With increasing RI of SiO₂, the high energy (“blue”) edge of the stop band shifts significantly, while the low energy (“red”) edge of the stop band is only slightly affected. In contrast, for changes in the RI of TiO₂, we observe a more significant shift of the “red” edge of the stop band, whereas the “blue” edge remains almost constant (Figure 2(d)). This observation can be generalized to arbitrary materials: a

change in RI of the low-RI material predominantly affects the “blue” edge, and a change in RI of the high-RI material significantly affects the “red” edge of the stop band, owing to the localization of the electromagnetic field in the high-dielectric material at the red edge of the stop band, and vice versa (Chen et al., 2006). Consequently, two conclusions can be drawn: first, even minute changes in the RIs of the layers at constant layer thickness have a major impact on the position, especially the width of the stop band. This generally translates into a high sensitivity to processes changing the effective RI of one or both of the layers, such as the adsorption of ambient humidity into a porous material (Pavlichenko et al., 2012), as evidenced by using NP-based layers with a high degree of textural porosity (note that by textural porosity, we refer to the porosity arising from intra-aggregate/interparticle voids in the film, i.e. from the spaces formed by interparticle contacts). Second, a BS sensing element may distinguish between a disproportionate change of the RIs of the two different layer materials, for instance, if one layer material shows a significantly larger porosity or TOC than the other layer material, leading to substantial changes in the RI contrast and hence the width of the stop band. Therefore, we may conclude that the observation of the asymmetrical shift for the BS in Figure 1 is consistent with the earlier simulations (Figure 2), indicating that the magnitude of the wavelength shift is larger for the “red” edge of the stop band due to the chosen wavelength scale. In addition, however, it can be seen that the width of the stop band in Figure 1 slightly decreases with increasing temperature, thus suggesting a disproportionate change of the RIs of the two different layer materials. The observed narrowing is in agreement with the scenario represented in Figure 2(d), indicating that the RI of TiO₂ changes more significantly than that of SiO₂ owing to larger amounts of physisorbed water in the more hydrophilic TiO₂ layers and a larger TOC of TiO₂.

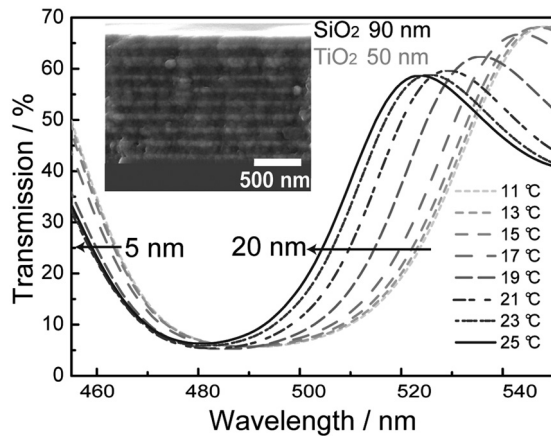


Figure 1. Transmission spectra of a 8.5-bilayer TiO_2 (50 nm)/ SiO_2 (90 nm) BS demonstrating a significant blue shift of the stop band in the temperature range between 15°C and 25°C at ambient conditions. Black bars indicate the shift of the “red” edge (20 nm) and of the “blue” edge (5 nm) of the stop band. The cross-sectional SEM image of the BS is shown in the upper left corner; the scale bar is 500 nm. BS: Bragg stack; SEM: scanning electron microscopy.

The basic design of BSs showing an enhanced thermo-optic response irrespective of ambient humidity is dominated by the choice of appropriate materials with a large TOC, as well as a suitable mutual enhancement of the TOCs of the individual layers. In order to outline the influence of the TOC of the two constituent layer materials, we have analyzed the thermo-optic response of two BS configurations with different material combinations.

We performed simulations for 9-bilayer 1D PCs based on TiO_2 and SiO_2 (Figure 3(a)) and on ZrO_2 and SiO_2 (Figure 3(b)). As outlined earlier, the TOC of TiO_2 is negative and equal to $-3 \times 10^{-4} \text{ K}^{-1}$, whereas the TOC of SiO_2 is positive and equal to $1 \times 10^{-5} \text{ K}^{-1}$. In the $\text{ZrO}_2/\text{SiO}_2$ combination, both TOCs are positive, and the TOC of ZrO_2 ($\approx 4.8 \times 10^{-4} \text{ K}^{-1}$) is roughly one order of magnitude larger than that of SiO_2 according to Inci et al. (1997). Owing to the larger TOCs of TiO_2 and ZrO_2 , the thermo-optic effect of the high-RI materials plays the dominant role in both configurations. In the $\text{TiO}_2/\text{SiO}_2$ BS, the stop band therefore shifts toward shorter wavelengths by 5 nm in the

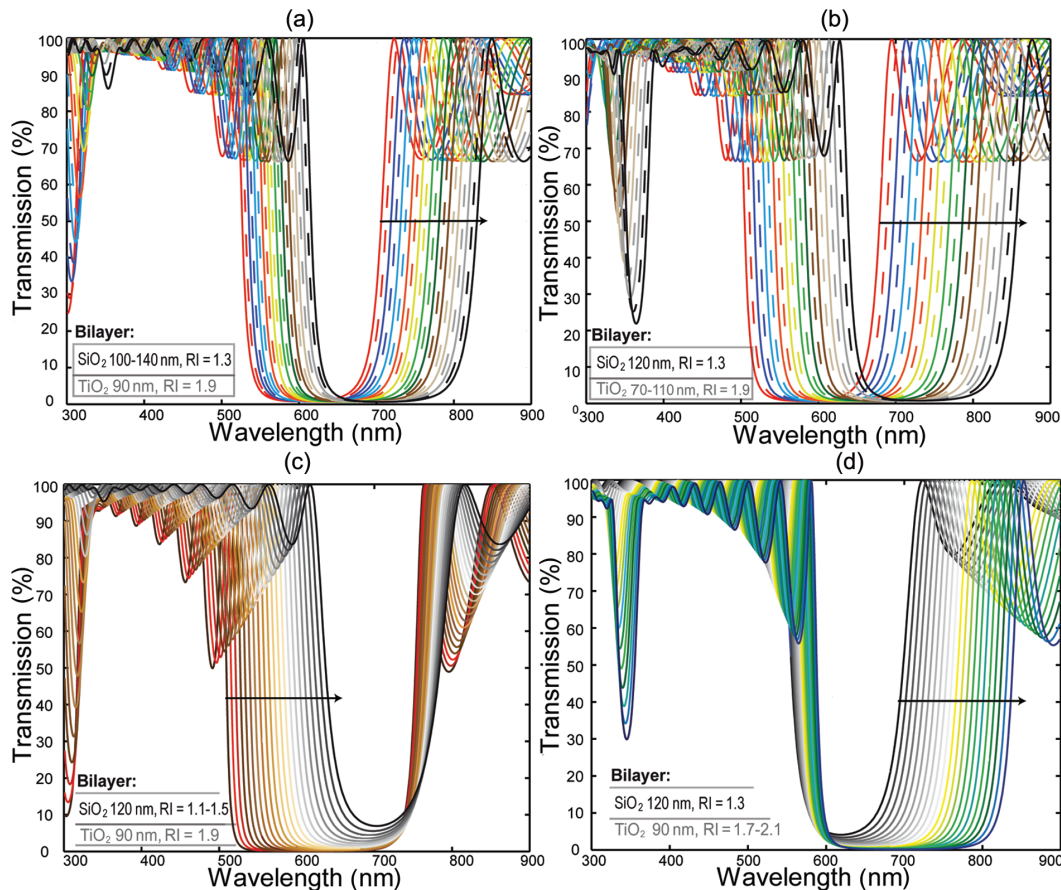


Figure 2. Simulated transmission spectra of a BS with 9-bilayer BSs, starting with the TiO_2 layer, and consisting of various combinations of (a) TiO_2 layers of 90 nm/RI = 1.9 and SiO_2 layers with RI = 1.3 and thicknesses varying from 100 to 140 nm. (b) TiO_2 layers with RI = 1.9 and thicknesses varying from 70 to 110 nm, and SiO_2 layers of 120 nm/RI = 1.3. (c) TiO_2 layers of 90 nm/RI = 1.9 and SiO_2 layers of 120 nm with RI varying from 1.1 to 1.5. (d) TiO_2 layers of 90 nm with RI varying from 1.7 to 2.1, and SiO_2 layers of 120 nm/RI = 1.3. The black arrow indicates the direction of the stop band shift as the layer thickness or RI increases. BS: Bragg stack; RI: refractive index.

temperature range between 10°C and 60°C; however, the positive TOC of silica counteracts this shifting behavior to some extent. In contrast, for the $\text{ZrO}_2/\text{SiO}_2$ BS, the thermal behavior shows the opposite trend in the same temperature range, and hence, the stop band is shifted to longer wavelengths. In addition, the shift is larger (8 nm), which can be explained by the same sign of the TOCs for both materials that therefore add up, leading to a larger thermo-optic response. Hence, we have verified the prediction implied in Figure 2 that in order to obtain a large thermo-optic response of a BS, both constituent materials need to have individually large TOCs, and both TOCs need to have the same sign. Note, however, that the amplifying effect on the temperature response by ambient humidity that is observed in the $\text{TiO}_2/\text{SiO}_2$ BS is expected to be reversed in the case of $\text{ZrO}_2/\text{SiO}_2$ BS, as the TOC (red shift with increasing temperature) and humidity response (blue shift with increasing temperature) would counteract each other.

Materials with large negative TOCs, such as polymers (Zhai et al., 2000) and hybrid organic/inorganic materials (Kurata et al., 2009), could be of interest for tunable thermo-optic PCs. However, their thermal expansion properties have to be taken into account. Since thermal expansion and negative TOCs may cancel out each other if the materials are assembled within a BS platform that only detects combined changes in the optical thickness, additional analysis of the influence of layer expansion would be needed.

The earlier simulations were done based on the thermo-optic response only, and humidity effects were

not explicitly accounted for. However, as has been shown above (Figure 1), the environmental conditions, especially ambient relative humidity (RH), have to be taken into account for porous films when designing a thermo-optic detection platform. Hence, one needs to account for the *effective* TOC of the layers including both thermal and humidity responses that can be measured, for example, by means of spectroscopic ellipsometry (Xie et al., 2008). Here, we analyze the influence of the bilayer lattice constant (the sum of the physical thicknesses of high-RI and low-RI materials) on the thermo-optic response of $\text{TiO}_2/\text{SiO}_2$ 1D PCs under environmental conditions, that is, using the effective TOCs and hence RIs determined for NP-based TiO_2 and SiO_2 thin films at RH = 25% (Pavlichenko et al., 2012). The effective TOC of the TiO_2 layer is given by $dn/dT = -1.61 \times 10^{-3} \text{ K}^{-1}$ between 10°C and 30°C at 25% RH and by $-2.52 \times 10^{-4} \text{ K}^{-1}$ above 30°C. The effective TOC of SiO_2 used for the simulations is also negative ($-2.52 \times 10^{-4} \text{ K}^{-1}$) over the whole temperature range and one order of magnitude larger than the literature values for dense layers. Figure 4(a) to (d) outlines the thermal shift between 10°C and 60°C for a 9-bilayer BS with the following bilayer combinations: (a) 50/80, (b) 50/90, (c) 60/90, (d) 50/110, and (e) 110/90 nm for $\text{TiO}_2/\text{SiO}_2$ layers, respectively, hence changing the lattice constant from (a) 130 to (e) 200 nm. It can be seen from the graphs that when detecting the shifts optically, that is, on the wavelength scale, larger shifts are observed for BSs with larger lattice constants and, hence, stop bands located at larger wavelengths. To explore the influence of the relative portions of the

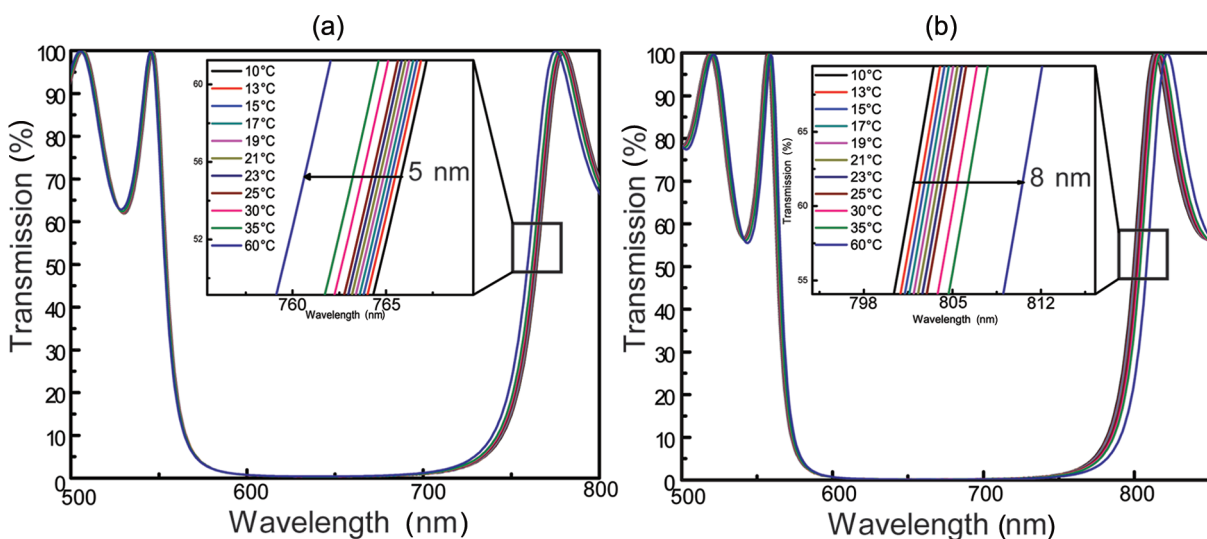


Figure 3. Simulated transmission spectra, demonstrating the thermal shift of the stop band in the range between 10°C and 60°C of two 9-bilayer BSs with TOCs as described in the text: (a) 90/120 nm $\text{TiO}_2/\text{SiO}_2$ and (b) 90/120 nm $\text{ZrO}_2/\text{SiO}_2$. The black arrow indicates the direction of the stop band shift toward (a) shorter wavelengths for negative (large)/positive (small) TOCs for $\text{TiO}_2/\text{SiO}_2$, respectively, and (b) longer wavelengths for positive (large)/positive (small) TOCs for $\text{ZrO}_2/\text{SiO}_2$, respectively. BS: Bragg stack; TOC: thermo-optic coefficient.

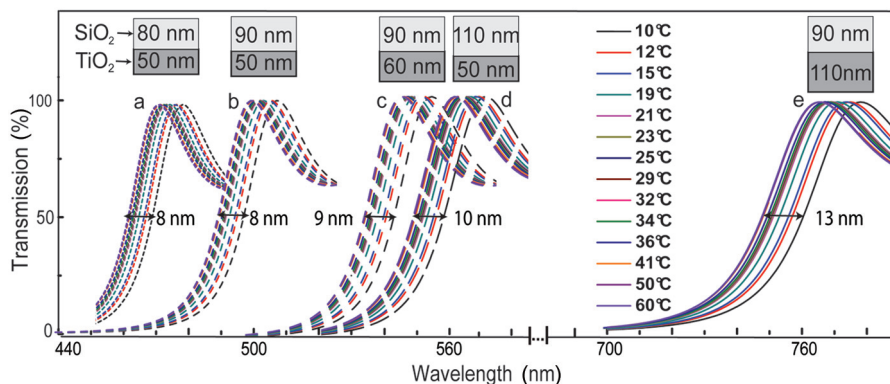


Figure 4. Simulated transmission spectra of a 9-bilayer BS, demonstrating the thermal shift of the stop band in the range between 10°C and 60°C with the experimental TOCs at 25% RH for TiO₂ and SiO₂ thin films and the following lattice parameters: (a) 50/80, (b) 50/90, (c) 60/90, (d) 50/110, and (e) 110/90 nm for the TiO₂/SiO₂ layers, respectively. The magnitude of the shift for each combination is indicated next to the black arrow.

BS: Bragg stack; TOC: thermo-optic coefficient; RH: relative humidity.

high-RI and low-RI materials in a bilayer with constant thickness, the ratio of the high-RI material (TiO₂) to the low-RI material (SiO₂) in a 9-bilayer BS was varied in a stepwise manner from 40/110 nm (Figure 5(a)) to 110/40 nm (Figure 5(b)) for TiO₂/SiO₂ with a constant bilayer thickness of 150 nm. A relative increase of the high-RI material portion shifts the stop band toward longer wavelengths and hence also increases the shift of the “red” edge of the stop band. In an optical detection mode, the most significant thermal response can therefore be observed for 1D PCs with a large bilayer thickness and/or a high portion of the high-RI material, as both conditions will increase the optical thickness of the BS and hence shift the position of the stop band to the red.

In the earlier simulations, we looked at the humidity-enhanced thermal shift (i.e. the shift induced by *both* TOC and ambient humidity, giving rise to an *effective* TOC) of the optical spectrum of the BS as a function of either cooling or heating and neglecting any affects attributable to the morphology of the BS. However, in real systems whose response is affected by processes such as water adsorption into porous layers, we would expect a hysteresis to occur when recording the optical response along a full heating-cooling cycle. Therefore, the optical response of a 9-bilayer (TiO₂ (60 nm)/SiO₂ (110 nm)) BS was studied at 25% RH by cycling the temperature up and down in steps of 2°C while measuring the transmission value at a constant wavelength (610 nm). After each set-point temperature was reached, the sample was equilibrated for another 60 s before the measurement was taken. As can be seen in Figure 6, a hysteresis is indeed observed over more than five cycles. Heating-cooling cycles recorded with longer delay times up to 900 s do not significantly change the shape of the hysteresis, thereby suggesting that the

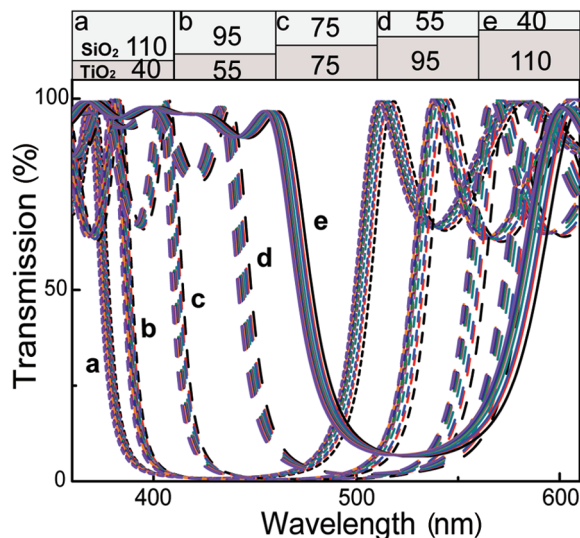


Figure 5. Simulated transmission spectra of a 9-bilayer BS, demonstrating the thermal shift of the stop band in the temperature range between 15°C and 60°C using the experimental TOCs at 25% RH for TiO₂/SiO₂ and the following layer thickness combinations at a fixed bilayer thickness of 150 nm: (a) 40/110, (b) 55/95, (c) 75/75, (d) 95/55, and (e) 110/40 nm. BS: Bragg stack; TOC: thermo-optic coefficient; RH: relative humidity.

water adsorption/desorption kinetics are fast and not responsible for the observed hysteresis. On the other hand, measurements under nitrogen atmosphere with exclusion of ambient humidity show no hysteresis, thus indicating that humidity is required in order for the hysteresis to occur. We assume that the hysteresis is due to capillary condensation of water into the textural mesopores of the layers resulting from the packing of the NPs, as is observed in similar thin film systems consisting of NPs (Demessence et al., 2010). In general, however, it can be noted that the

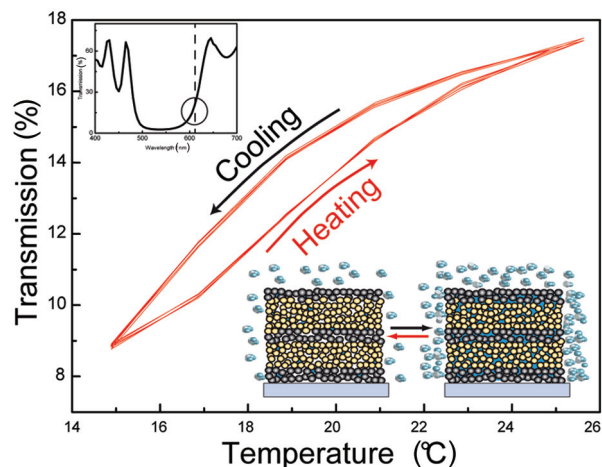


Figure 6. Heating and cooling curves recorded by monitoring the transmission at 610 nm and 25% RH between 15°C and 25°C. The stop band of the investigated BS is placed in the upper left corner. The temperature was cycled five times from 15°C to 25°C in steps of 2°C and backward with an equilibration time for each temperature of 60 s. The hysteresis may be caused by capillary condensation of ambient humidity into the mesoporous network of the BS as is schematically shown in the illustration (bottom right).

BS: Bragg stack; TOC: thermo-optic coefficient; RH: relative humidity.

maximum opening of the hysteresis loop is only about 1.5% in transmission at 25% RH and hence results in only a moderate, yet reproducible correction of the shifts expected for a purely thermo-optic response.

A crucial aspect in designing an optical device that can detect subtle changes in RH and temperature is the average response time. The thermal response is expected to be fast if the BS is in thermal equilibrium with its environment. Therefore, although we have shown earlier that the adsorption/desorption kinetics is faster than about 60 s, we infer that the response time is still dominated by the uptake of ambient humidity into the porous BS architecture. In Figure 7, we outline an experiment that allows for a simple characterization of the response time of the multilayer system with respect to changes in ambient humidity, while keeping the temperature constant. In a typical experiment, the BS (9-bilayer TiO₂, 60 nm, 10% porosity/SiO₂, 100 nm, 25% porosity) was fixed under a microscope (20% RH at 20°C) such that the measurement spot could be constantly monitored. Then, time-resolved measurements were carried out detecting changes in transmission occurring during the external change in RH of the environment, provided by a flow setup, from 20% to 70%. Upon increasing RH, humidity is adsorbed into the textural mesopores of the BS, thus increasing the RI of the materials comprising the BS and shifting the stop band to larger wavelengths. For the BS in Figure 7(a), the transmission at 450 nm was monitored during the humidity change as shown in Figure 7(d) and (e). The

response time $\langle\tau_1\rangle$ to the humidity change was ascertained to be 2 s, and the recovery time $\langle\tau_2\rangle$ after turning down the water vapor flow is approximately equal to 3.8 s, both being significantly longer than the response times of the materials due to the thermo-optic effect alone ($\sim 10^{-6}$ – 10^{-3} s; Coppola et al., 2011; Haché and Allogho, 2011). The difference in the response and recovery times can be associated with the kinetics of the adsorption and desorption processes, where desorption is slightly more sluggish and proceeds in two steps. We also fabricated a BS (4-bilayer TiO₂, 45 nm, 10% porosity/SiO₂, 60 nm, 40% porosity) with a higher porosity of the SiO₂ layers, as can be seen in Figure 8(a) and (b). Again, the transmission change at 500 nm was monitored during abrupt changes in environmental RH from 20% to 70% (Figure 8(c) and (d)). Although the number of bilayers for this BS is almost two times less than that of the BS as shown in Figure 7 and additional porosity was introduced into the system, the response time $\langle\tau_1\rangle$ is only slightly smaller, being equal to 1.5 s (recovery time $\langle\tau_2\rangle \approx 3$ s). Colodrero et al. (2008b) associated this phenomenon with the fact that the sorption properties of the stack are determined by the interaction between the neighboring layers, and the response is mediated by the layer with smaller pores, which in our case is the TiO₂ NP layer in both BS configurations. Accordingly, further titania layer modification toward higher porosity would be required for even faster response times. In general, however, the observed fast response times can be of interest, for example, in medical applications where fast sampling of a patient's breathing may be required, since human expiration contains large amounts of water vapor compared to ambient air (Arregui et al., 2000).

Conclusion

In this study, we present a comprehensive analysis of thermoresponsive TiO₂/SiO₂ BSs assembled by a sol-gel fabrication process. We demonstrate that due to the porous nature of the multilayer system, the temperature response of such systems is significantly enhanced in the presence of ambient humidity. In order to gain insights into the BS response to temperature and humidity, both acting on the effective RI of the multilayer system, we carried out simulations detailing the influence of RI, TOC, and layer thicknesses on the stop band position and width as well as temperature sensing characteristics. A high thermo-optic response that can be read out optically is expected for material combinations with large bilayer thicknesses, high RI contrast, and large TOCs having the same sign. As the width of the stop band is a sensitive probe of the relative RI changes of the two layer materials, it should be possible to predict the material that is affected the most by humidity-induced RI changes.

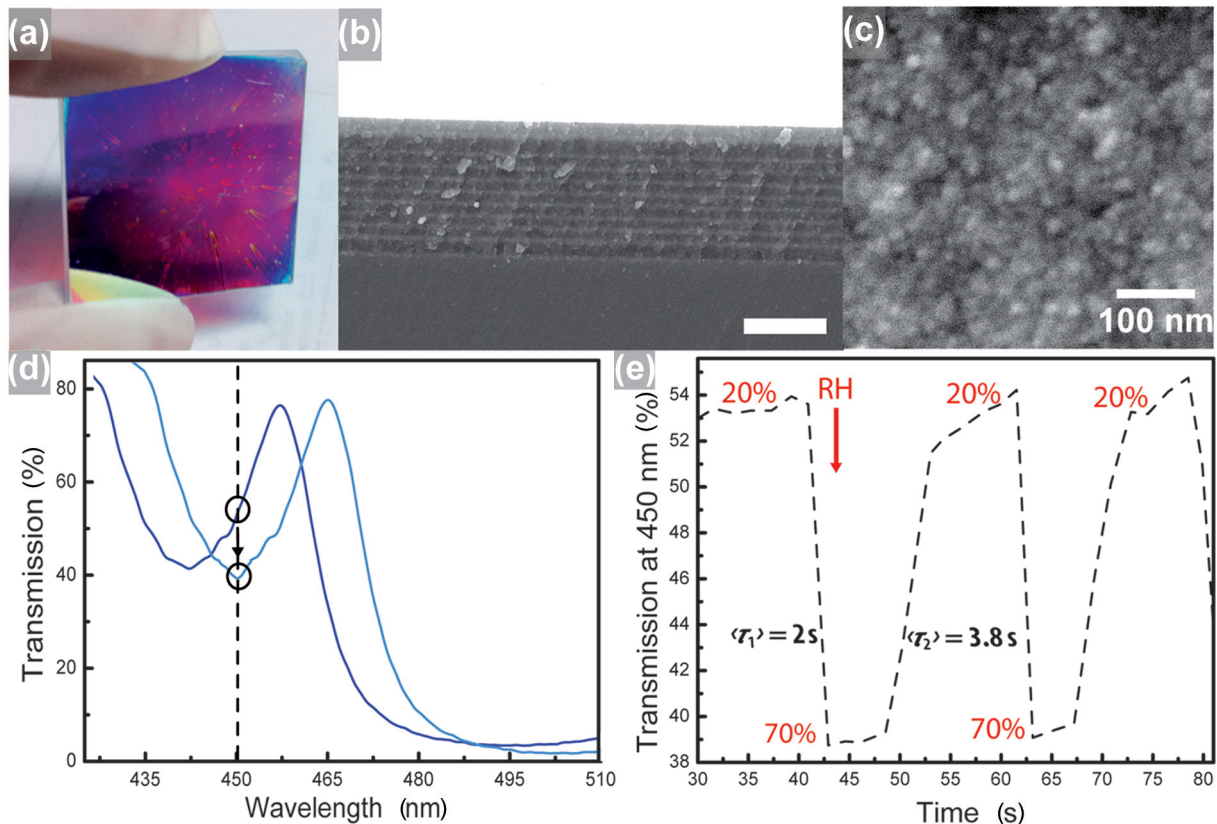


Figure 7. (a) Photograph of a 9-bilayer TiO_2 (60 nm)/ SiO_2 (100 nm) ID PC fabricated on a $2.5 \times 2.5\text{ cm}^2$ glass slide by multiple spin-coating, (b) SEM image of the cross section of the BS (scale bar is $1\ \mu\text{m}$), (c) SEM image showing the morphology of the TiO_2 top layer of the BS, (d) transmission spectra of the BS demonstrating the change in the transmission at 450 nm corresponding to the RH change from 20% to 70%, and (e) time-resolved transmission change in response to the change of the RH from 20% to 70%. $\langle \tau_1 \rangle$ is the response time to the increase in humidity, and $\langle \tau_2 \rangle$ is the recovery time after the end of the stimulus (i.e. upon decrease in humidity).

ID PC: one-dimensional photonic crystal; SEM: scanning electron microscopy; BS: Bragg stack; RH: relative humidity.

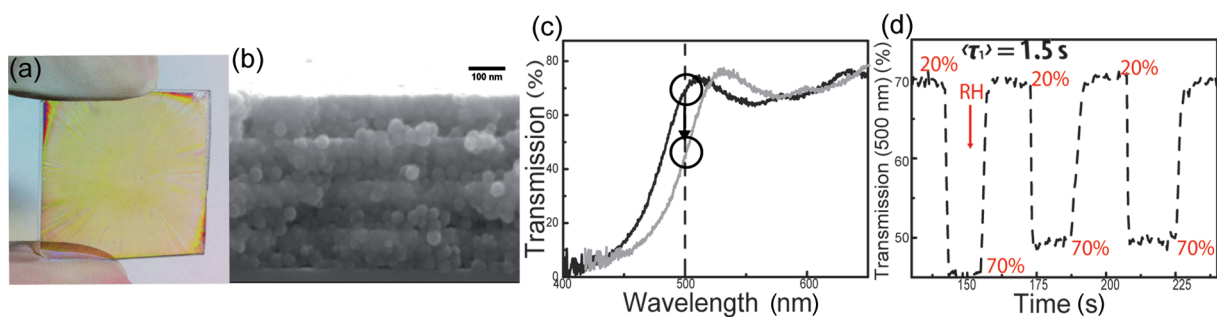


Figure 8. (a) Photograph of a 4-bilayer TiO_2 (45 nm)/ SiO_2 (60 nm) ID PC possessing higher porosity of the SiO_2 layer (40%), fabricated on a $2.5 \times 2.5\text{-cm}^2$ glass slide by multiple spin-coating, (b) SEM image of the cross section of the BS (scale bar is 100 nm), (c) transmission spectra of the BS demonstrating the change in the transmission at 500 nm corresponding to the RH change from 20% to 70%, and (d) time-resolved transmission change in response to the change of the RH from 20% to 70%. $\langle \tau_1 \rangle$ is the response time to the increase in humidity.

ID PC: one-dimensional photonic crystal; SEM: scanning electron microscopy; BS: Bragg stack; RH: relative humidity.

The investigated BSs show an amplified thermal response when exposed to ambient humidity, suggesting that water is adsorbed in the textural mesopores,

thus altering the effective RI of the constituent materials. This assumption was supported by subjecting the BS to several heating-cooling cycles, resulting in a

hysteresis loop for temperatures between 15°C and 25°C with a maximum opening of 1.5% in transmission at 19°C, which is consistent with capillary condensation of water inside the mesopores. Fast response times of approximately 2–4 s upon exposure to different humidity environments are testament to a fast water adsorption/desorption kinetics that bodes well for the use of such systems as sensitive temperature and humidity detection platforms.

Funding

This study was supported by the cluster of excellence Nanosystems Initiative Munich (NIM) as well as the Center for Nanoscience (CeNS). The doctoral scholarships for Ida Pavlichenko and Armin Exner are granted by the Elite Network of Bavaria and the International Graduate School of Science and Engineering (IGSSE), respectively.

References

- Arregui FJ, Cooper KL, Liu Y, et al. (2000) Optical fiber humidity sensor with a fast response time using the ionic self-assembly method. *IEICE Transactions on Electronics* E83-C(3): 360–365.
- Bonifacio LD, Lotsch BV, Puzzo DP, et al. (2009) Stacking the nanochemistry deck: structural diversity in one-dimensional photonic crystals. *Advanced Materials* 21: 1641–1646.
- Calvo ME, Colodrero S, Hidalgo N, et al. (2011) Porous one dimensional photonic crystals: novel multifunctional materials for environmental and energy applications. *Energy & Environmental Science* 4: 4800–4812.
- Calvo ME, Colodrero S, Rojas C, et al. (2008) Photoconducting Bragg mirrors based on TiO₂ nanoparticle multilayers. *Advanced Functional Materials* 18(18): 2708–2715.
- Chen JIL, Von Freymann G, Choi SY, et al. (2006) Amplified photochemistry with slow photons. *Advanced Materials* 18: 1915–1919.
- Colodrero S, Ocanã M and Míguez H (2008a) Nanoparticle-based one-dimensional photonic crystals. *Langmuir* 24: 4430–4434.
- Colodrero S, Ocanã M, González-Elipse AR, et al. (2008b) Response of nanoparticle-based one-dimensional photonic crystals to ambient vapor pressure. *Langmuir* 24: 9135–9139.
- COMSOL Multiphysics (2008) RF module model library version 3.5. Available at: <http://www.comsol.com/>
- Coppola G, Sirtelo L, Rendina I, et al. (2011) Advance in thermo-optical switches: principles, materials, design, and device structure. *Optical Engineering* 50(7): 071112-071112-14.
- Demessence A, Boissière C, Grosso D, et al. (2010) Adsorption properties in high optical quality nanoZIF-8 thin films with tunable thickness. *Journal of Materials Chemistry* 20: 7676–7681.
- Domash LH, Ma EY, Lourie MT, et al. (2003) Broadly tunable thin film interference coatings: active thin films for telecom applications. *Proc. SPIE 4989*: vol. 4989. pp. 161–167.
- Ge J and Yin Y (2011) Responsive photonic crystals. *Angewandte Chemie International Edition* 50: 1492–1522.
- Ghosh G (1995) Model for the thermo-optic coefficients of some standard optical glasses. *Journal of Non-Crystalline Solids* 189: 191–196.
- Gülşen G and Inci MN (2002) Thermal optical properties of TiO₂ films. *Optical Materials* 18: 373–381.
- Haché A and Allogho GG (2011) Opto-thermal modulation in biological photonic crystals. *Optics Communication* 284: 1656–1660.
- Hench LL and West JK (1990) The sol-gel process. *Chemical Reviews* 90(1): 33–72.
- Hohlfeld D and Zappe H (2004) An all-dielectric tunable optical filter based on the thermo-optic effect. *Journal of Optics A-Pure and Applied Optics* 6: 504–511.
- Inci MN, Gülşen G, Yaradanakul MA, et al. (1997) Experimental determination of the thermo-optic properties of zirconium dioxide coating. *Journal of Physics D-Applied Physics* 30: 517–521.
- Inui C, Tsuge Y, Kura H, et al. (2008) Preparation of one-dimensional photonic crystals by sol-gel process for magneto-optical materials. *Thin Solid Films* 516(9): 2454–2459.
- Joannopoulos JD, Johnson SG, Winn JN, et al. (2008) *Photonic Crystals: Molding the Flow of Light*. 2nd ed. Princeton, NJ: Princeton University Press, pp. 44–65.
- Kobler J, Lotsch BV, Ozin GA, et al. (2009) Vapor-sensitive Bragg mirrors and optical isotherms from mesoporous nanoparticle suspensions. *ACS Nano* 3:1669–1676.
- Kurata Y, Sugihara O, Kaino T, et al. (2009) Thermo-optic controllable hybrid photonic polymers containing inorganic nanoparticles. *Journal of the Optical Society of America B-Optical Physics* 26(12): 2377–2381.
- Lee D, Rubner MF and Cohen RE (2006) All-nanoparticle thin-film coatings. *Nano Letters* 6: 2305–2312.
- Lotsch BV and Ozin GA (2008) Photonic clays: a new family of functional 1D photonic crystals. *ACS Nano* 2: 2065–2074.
- Lotsch BV, Knobbe CB and Ozin GA (2009) A step towards optically encoded silver release in 1D photonic crystals. *Small* 5: 1498–1503.
- Macwan DP, Dave PN and Chaturvedi S (2011) A review on nano-TiO₂ sol-gel type syntheses and its applications. *Journal of Materials Science* 46: 3669–3686.
- Nogueira GM, Banerjee D, Cohen RE, et al. (2011) Spray-layer-by-layer assembly can more rapidly produce optical-quality multistack heterostructures. *Langmuir* 27: 7860–7867.
- Park JK and Kim HK (2002) Preparation and characterization of hydrophilic TiO₂ film. *Bulletin of the Korean Chemical Society* 23(5): 745–748.
- Patzke GR, Zhou Y, Kontic R, et al. (2011) Oxide nanomaterials: synthetic developments, mechanistic studies, and technological innovations. *Angewandte Chemie-International Edition* 50: 826–859.
- Pavlichenko I, Exner AT, Guehl M, et al. (2012) Humidity-enhanced thermally tunable TiO₂/SiO₂ Bragg stacks. *Journal of Physical Chemistry C* 116(1): 298–305.
- Puzzo DP, Helander MG, O'Brien PG, et al. (2011) Organic light-emitting diode microcavities from transparent conducting metal oxide photonic crystals. *Nano Letters* 11(4): 1457–1462.
- Redel E, Mirtchev P, Huai C, et al. (2011) Nanoparticle films and photonic crystal multilayers from colloiddally stable,

- size-controllable zinc and iron oxide nanoparticles. *ACS Nano* 5(4): 2861–2869.
- Sánchez-Sobrado O, Calvo ME and Míguez H (2010) Versatility and multifunctionality of highly reflecting Bragg mirrors based on nanoparticle multilayers. *Journal of Materials Chemistry* 20: 8240–8246.
- Sánchez-Sobrado O, Lozano G, Calvo ME, et al. (2011) Interplay of resonant cavity modes with localized surface plasmons: optical absorption properties of Bragg stacks integrating gold nanoparticles. *Advanced Materials* 23(18): 2108–2112.
- Scotognella F, Puzzo DP, Monguzzi A, et al. (2009) Nanoparticle one-dimensional photonic-crystal dye laser. *Small* 5(18): 2048–2052.
- Tai WP, Kima JG and Oh JH (2003) Humidity sensitive properties of nanostructured Al-doped ZnO:TiO₂ thin films. *Sensors and Actuators B-Chemical* 96: 477–481.
- Tsuchiya T, Emoto T and Sei T (1994) Preparation and properties of transparent conductive thin films by the sol-gel process. *Journal of Non-Crystalline Solids* 178: 327–332.
- Wu Z, Lee D, Rubner MF, et al. (2007) Structural color in porous, superhydrophilic, and self-cleaning SiO₂/TiO₂ Bragg stacks. *Small* 3(8): 1445–1451.
- Xie H, Zeng XT and Yeo WK (2008) Temperature dependent properties of titanium oxide thin films by spectroscopic ellipsometry. *SIMTech Technical Reports* 9: 29–32.
- Yadav BC, Pandey NK, Srivastava AK, et al. (2007) Optical humidity sensors based on titania films fabricated by sol-gel and thermal evaporation methods. *Measurement Science & Technology* 18: 260–264.
- Yu J, Zhao X, Zhao G, et al. (2001) Preparation and characterization of super-hydrophilic porous TiO₂ coating films. *Materials Chemistry and Physics* 68: 253–259.
- Zhai J, Qiu L, Zhou J, et al. (2000) Study on the thermal properties of doped PMMA systems. *Advanced Materials for Optics and Electronics* 10: 3–7.
- Zverev GM, Sidoryuk OE and Skvortsov LA (1981) Influence of water adsorption processes on the optical strength of dielectric titanium dioxide coatings. *Sov. J. Quantum Electron* 11(10): 1393–1395.